

## Supporting Information

### **Thermodynamic and Dynamic Dual Regulation Bi<sub>2</sub>O<sub>2</sub>CO<sub>3</sub>/ Bi<sub>5</sub>O<sub>7</sub>I Enabling High-flux Photogenerated Charge Migration for Enhanced Visible-light-driven Photocatalysis**

Yan Guo<sup>a</sup>, Jun Nan<sup>a</sup>, Yongpeng Xu<sup>a</sup>, Fuyi Cui<sup>b</sup>, Wenxin Shi<sup>a,b</sup>\*, and Yongfa Zhu<sup>c</sup>\*

<sup>a</sup> State Key Laboratory of Urban Water Resource and Environment, School of Environment, Harbin Institute of Technology, Harbin 150090, China

<sup>b</sup> School of Environment and Ecology, Chongqing University, Chongqing, 400044, China

<sup>c</sup> Department of Chemistry, Tsinghua University, Beijing, 100084, China

\*Corresponding author. E-mail: swx@hit.edu.cn, zhuyf@tsinghua.edu.cn

# Contents

<b>1. Supporting figures</b> .....	3
<b>1.1 Support for thermodynamic and kinetic conditions for BOC/BOI heterojunction (Figure S1-S3)</b> 3	
<b>1.2 Theoretical support for Bi-O chemical bonds at the interface (Figure S4-S7)</b> .....	7
<b>1.3 Characterization of Bi<sub>2</sub>O<sub>2</sub>CO<sub>3</sub>/Bi<sub>5</sub>O<sub>7</sub>I-2 (Figure S8-S10)</b> .....	11
<b>1.4 Performance evaluation of photocatalytic degradation for as-prepared samples (Figure S11-S16)</b> .....	15
<b>1.5 Identification for the intermediates of BPA degradation in Bi<sub>2</sub>O<sub>2</sub>CO<sub>3</sub>/Bi<sub>5</sub>O<sub>7</sub>I-2 system under <math>\lambda \geq 420</math> nm irradiation (Fig. S17)</b> .....	22
<b>1.6 Support for carrier lifetime of Bi<sub>2</sub>O<sub>2</sub>CO<sub>3</sub>/Bi<sub>5</sub>O<sub>7</sub>I-2 (Figure S18)</b> .....	27
<b>1.7 Schematic diagram of BOC / BOI heterojunction efficient photocatalysis (Figure S19)</b> .....	28
<b>2. Supporting tables</b> .....	29
<b>3. Reference</b> .....	35

## 1. Supporting figures

### 1.1 Support for thermodynamic and kinetic conditions for BOC/BOI heterojunction

(Figure S1-S3)

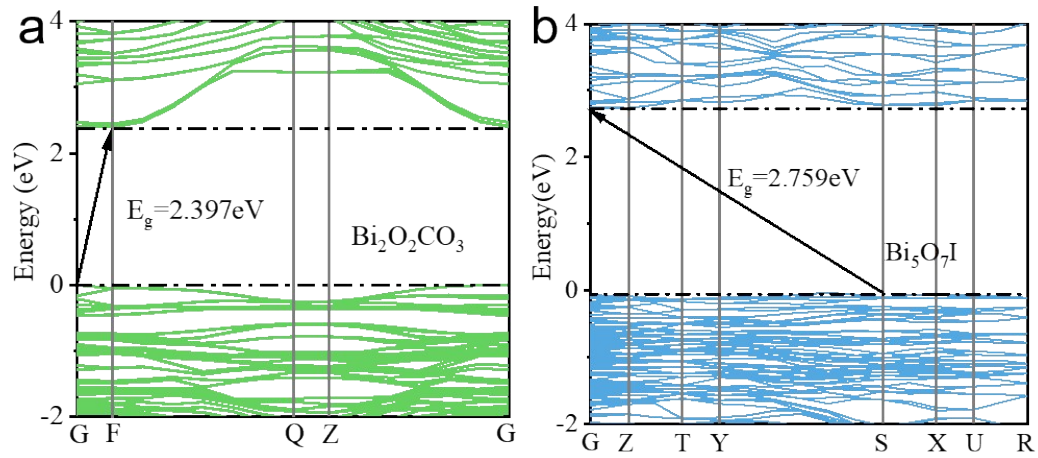


Figure S1. Calculated band structure of individual (a) BOC and (b) BOI.

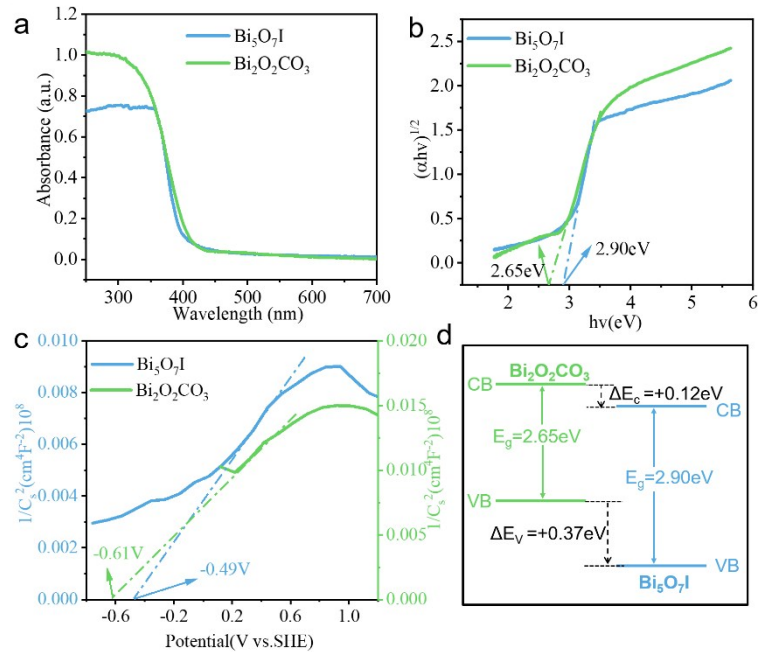


Figure S2. (a) UV-vis diffuse reflection spectra and (b) Plots of the transformed Kubelka–Munk function vs. the light energy (c) Mott-Schottky plots and (d) band alignment of BOC/BOI.

The information available from Figure S2 is as follows:

The UV-vis diffuse reflection data (Figure S2a) reflects the forbidden band widths of BOC and BOI are 2.65 eV and 2.90 eV, respectively, which is accord with the trend of DFT results (Figure S1).

Band gap:  $E_{g-BOI}=2.90\text{eV}$ ,  $E_{g-BOC}=2.65\text{eV}$ ,

The difference in band gap width is  $\Delta E_g=E_{g-BOI}-E_{g-BOC}=2.90-2.65=0.25\text{eV}$

The Position of conduction band (vs. SHE):  $E_{c-BOI}=-0.49\text{eV}$ ,  $E_{c-BOC}=-0.61\text{eV}$

The Position of valence band (vs. SHE):

$$E_{v-BOI}=E_{g-BOI}+E_{c-BOI}=2.90+(-0.49)=2.41\text{eV}$$

$$E_{v-BOC}=E_{g-BOC}+E_{c-BOC}=2.65+(-0.61)=2.04\text{eV}$$

The conduction band offset is calculated according to the position of the conduction band:

$$\Delta E_c=E_{c-BOI}-E_{c-BOC}=-0.49-(-0.61)=+0.12\text{eV}$$

The valence band offset is calculated according to the position of the valence band:

$$\Delta E_v = E_{v\text{-BOI}} - E_{v\text{-BOC}} = 2.41 - 2.04 = +0.37 \text{ eV}$$

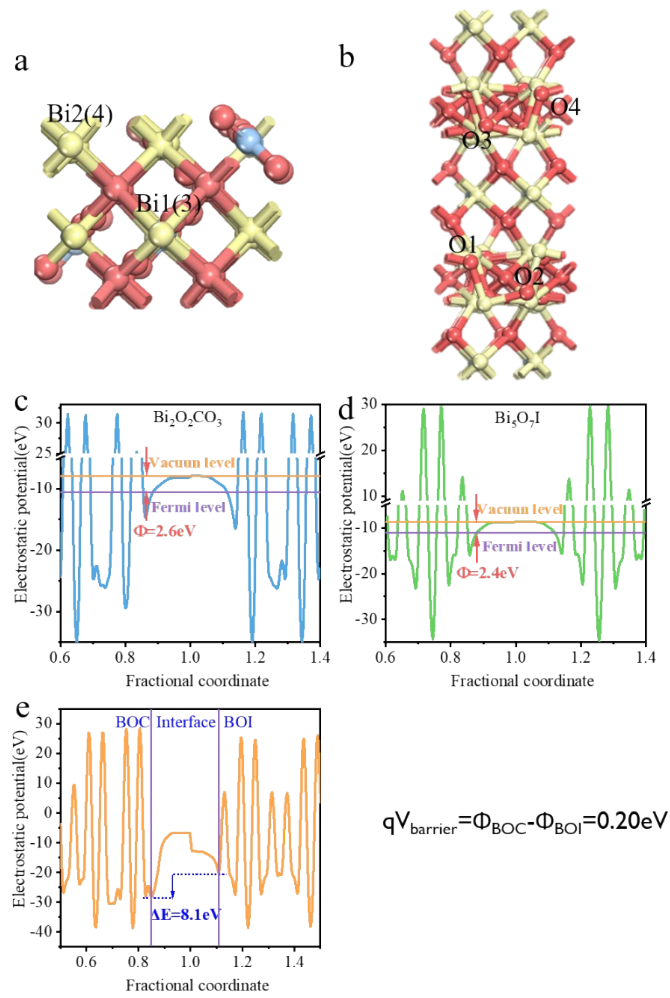


Figure S3. Simulation models for BOC/BOI interface: (a) BOC and (b) BOI. Potential lineup diagrams of BOC and BOI near the surface: (c) BOC (0 10 0) surface, (d) BOI (0 0 4) surface, and (e) BOC (0 10 0)–BOI (0 0 4) interface. The barrier ( $qV_{\text{barrier}}$ ) was calculated as the sum of the potential difference between two bare materials without interactions and the potential difference at the interface, in which interfacial interactions (i.e., dipole formation and geometry relaxation) were taken into account in the first-principles simulations.

## 1.2 Theoretical support for Bi-O chemical bonds at the interface (Figure S4-S7)

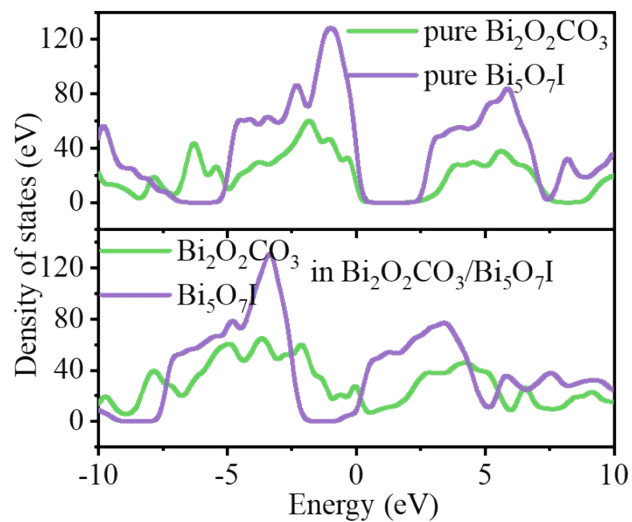


Figure S4. PDOS diagrams of pure BOC, BOI and BOC-BOI interface from first-principles simulations.

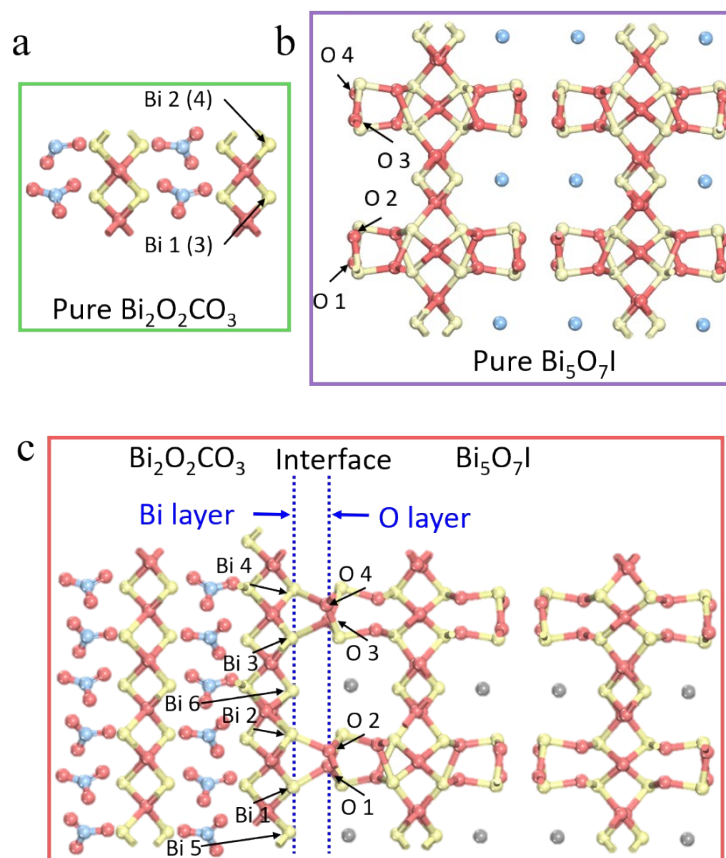


Figure S5. Crystal structure model comparison before and after the interface is formed: (a) pure BOC, (b) pure BOI and (c) BOC/ BOI.

The optimization model diagram of the heterojunction formed by BOC (0 10 0) and BOI (0 0 4) shows that the interface is composed of Bi atoms exposed by BOC and a small amount of O atoms exposed by BOI. The chemical environment and geometrical position of the Bi layer in BOC at the interface are almost unchanged, but the O layer in BOI changes significantly. Therefore, we choose to compare the static charge difference of the Bi layer in BOC at the interface before and after the heterojunction to explain the interface charge distribution next.



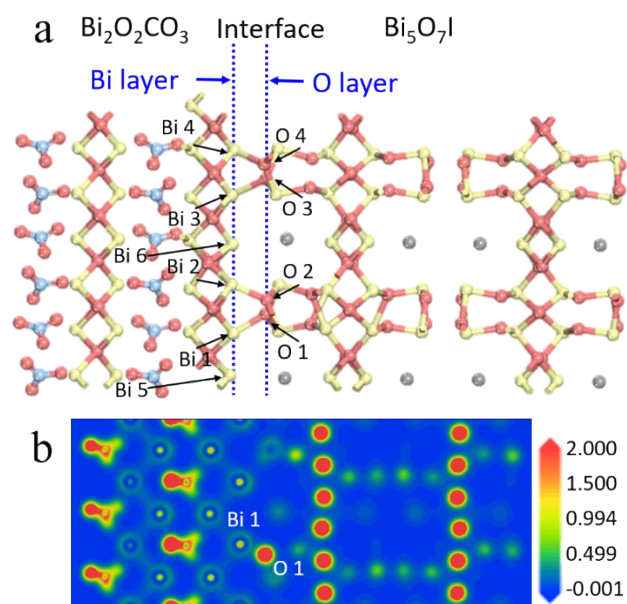


Figure S6. (a) Crystal structure illustrations of BOC/BOI (sphere color: blue, carbon; yellow, bismuth; red, oxygen; gray, iodine). (b) The charge density contour of the plane where Bi 1 and O 1 are located.

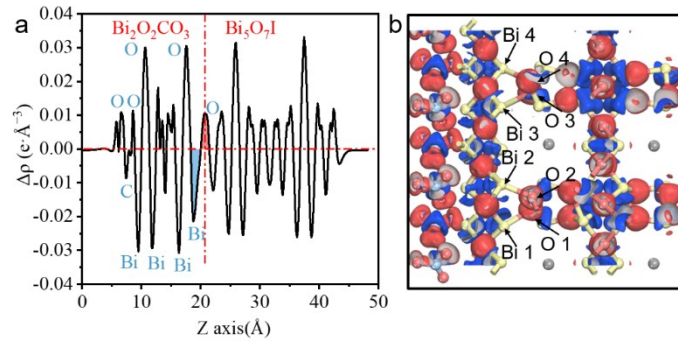


Figure S7. (a) Charge density difference map and (b) charge density difference isosurface

$$(\Delta\rho=0.07e\cdot\text{\AA}^{-3})$$

Figure S7a shows the average charge density in the plane along the composite Z-axis. Red represents electron accumulation and blue represents electron depletion. It can be seen that Bi-O has obvious electron accumulation and depletion at the interface. Nevertheless, the degree of charge transfer between Bi and O at the interface is lower than that of the bulk phase, which is due to the larger spacing of Bi-O layers at the interface (1.93 Å) than that in the bulk phase (1.12 Å). At the same time, the three-dimensional differential charge density (Figure S7b) visually shows the state of Bi 1~4 electron depletion of BOC at the interface and the O1~4 electron accumulation of BOI, indicating that there is strong electron coupling at the heterojunction interface.

### 1.3 Characterization of $\text{Bi}_2\text{O}_2\text{CO}_3/\text{Bi}_5\text{O}_7\text{I}$ -2 (Figure S8-S10)

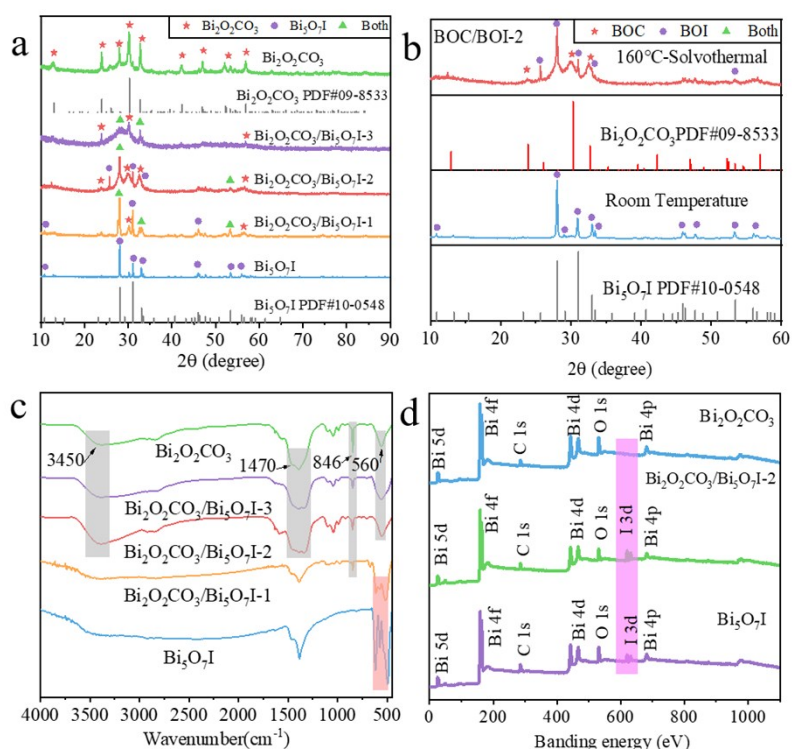


Figure S8. (a) XRD patterns of as-prepared samples. (b) XRD pattern of BOC/BOI-2 produced at 160°C solvothermal and room temperature. (c) FT-IR spectra and (d) XPS survey spectrum of as-prepared samples.

First, the crystal structure of the prepared samples was analyzed by XRD. It can be seen from Figure S8a that the characteristic peaks of BOC and BOI can be observed in prepared composite BOC/BOI-1, BOC/BOI-2 and BOC/BOI-3, indicating the successful synthesis of the two-phase composite structure. The intensity of BOC diffraction peak at 28.90° increased in turn, indicating that the amount of BOC in the composite samples was gradually increased. In addition, the relative intensity of the diffraction peaks of BOI changes because BOC is grown in situ on BOI, the diffraction intensity is weakened as the growth crystal plane turns into a short-range order.

In order to prove that BOC is produced by in-situ conversion on BOI, the XRD prepared under

normal temperature and hydrothermal conditions is as shown in Figure S8b. The precipitate produced at normal temperature is pure BOI, after 160 °C hydrothermal, there are significant BOC and BOI diffraction peaks due to the oxidation of glycerol to carbonate under autogenous pressure, followed by electrostatic interaction with the BOI surface and in situ conversion of BOI to BOC.

The formation of BOC/BOI composite was further identified by Fourier transform infrared spectroscopy (FT-IR) (Figure S8c). For pure BOC, the broad peak at 1470  $\text{cm}^{-1}$  and the peak at 846  $\text{cm}^{-1}$  correspond to the antisymmetric tensile vibration mode and bending mode of the  $\text{CO}_3^{2-}$  group,<sup>1</sup> and the peak at 560  $\text{cm}^{-1}$  is attributed to Bi-O in BOC.<sup>2</sup> The tensile vibration of the bond and a strong -OH peak at 3450  $\text{cm}^{-1}$  were formed due to the better water absorption of the sample surface. For pure BOI, the peak of Bi-O is between 500 and 620  $\text{cm}^{-1}$ , and there is no obvious water adsorption peak. For the BOC/BOI composite, the characteristic peak of BOC gradually becomes stronger as the the proportion of carbon source increases, indicating that a larger amount of BOC has formed.

The survey spectrum of XPS (Figure S8d) reveals that there are three elements B, O and C in the prepared BOC and there are three elements B, O and I in BOI. However, for the BOC coupled BOI sample, Bi, O, C, I four elements is present, indicating the formation of two-phase structure.

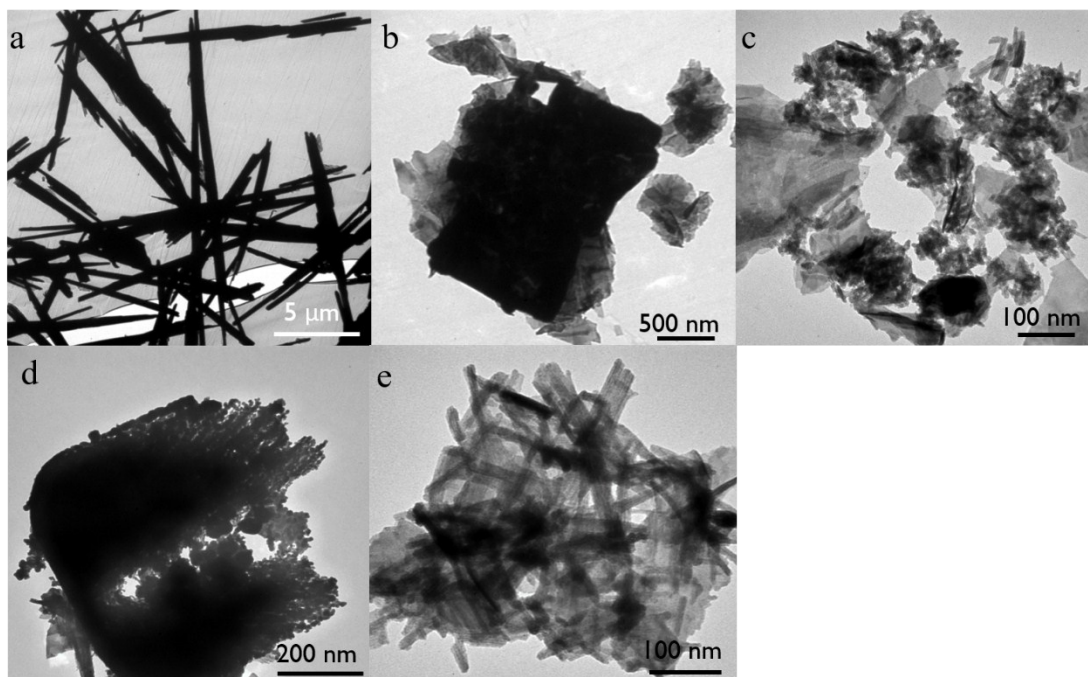


Figure S9. TEM of BOI (a), BOC/BOI-1 (b) BOC/BOI-2 (c) BOC/BOI-3 (d) BOC (e).

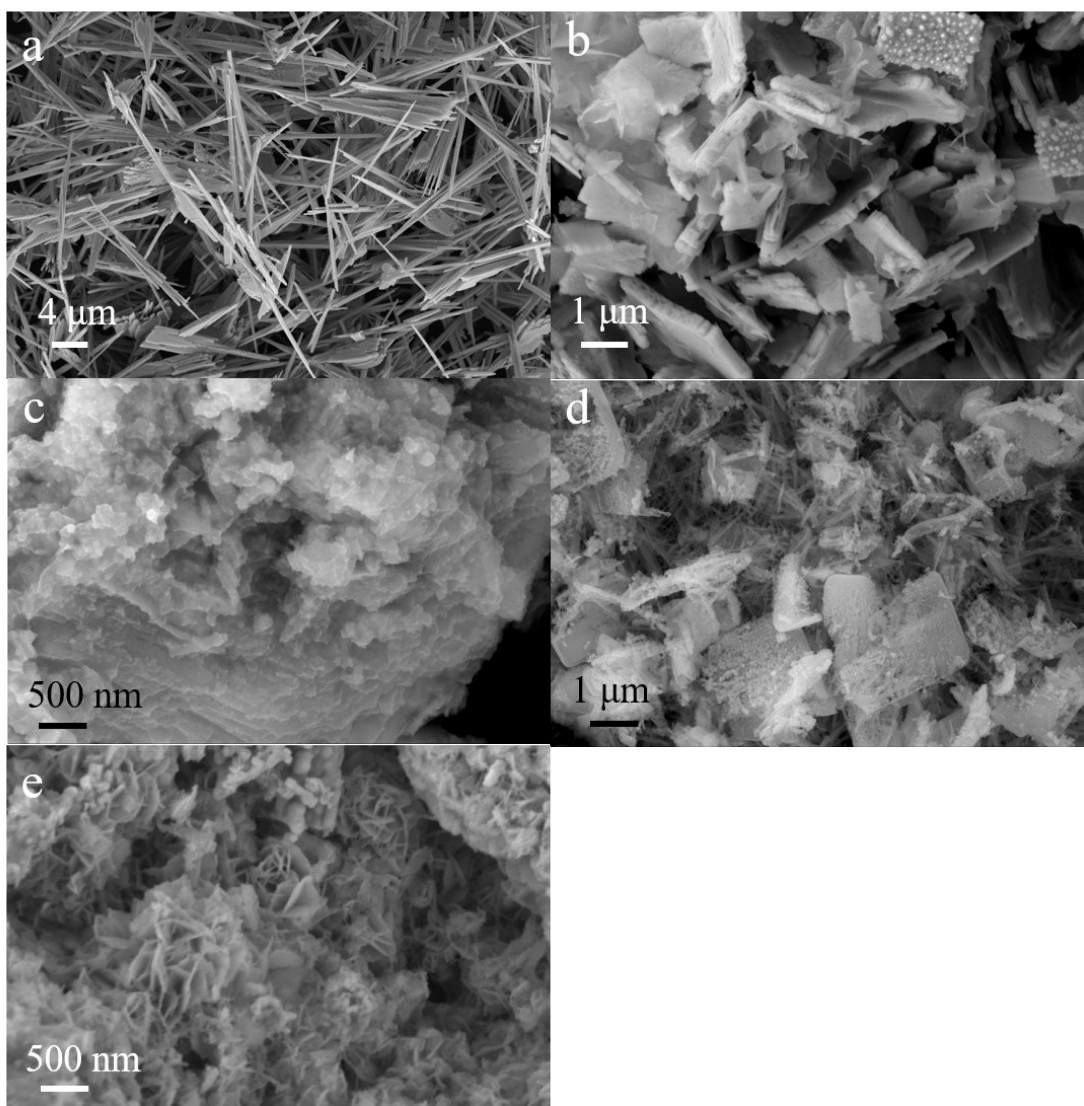


Figure S10. SEM of BOI (a), BOC/BOI-1 (b) BOC/BOI-2 (c) BOC/BOI-3 (d) BOC (e).

The heterojunction formed by few carbon sources is in the micron scale (Figure S9b and Figure S10b). In contrast, excessive carbon source cause BOI corroded and BOC increased resulting serious agglomeration (Figure S10d and Figure S10d). The pure BOC is a tremella-like patch without iodine source (Figure S10e and Figure S10e).

## 1.4 Performance evaluation of photocatalytic degradation for as-prepared samples

(Figure S11-S16)

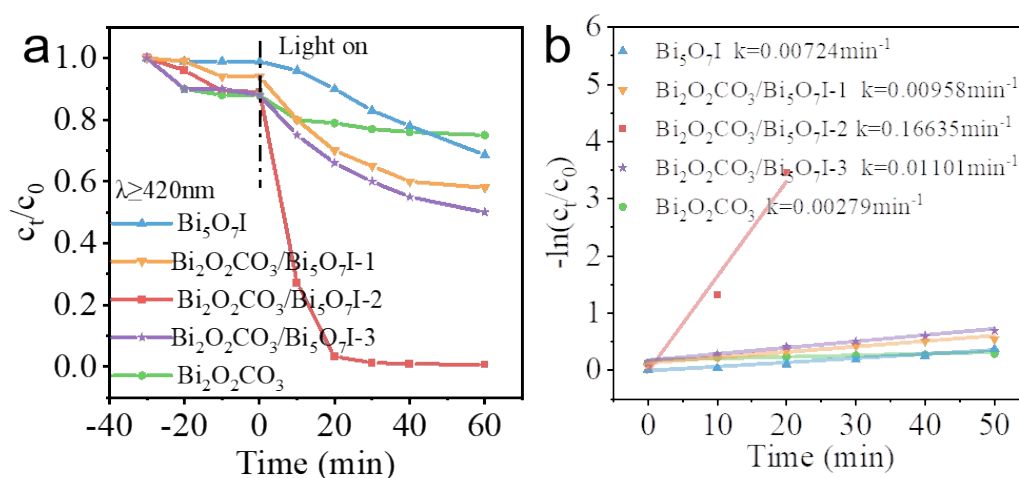


Figure S11. (a) Photocatalytic degradation for BPA under visible light ( $\lambda \geq 420\text{nm}$ ) irradiation and (b) pseudo first order kinetic fitting and the determined apparent rate constants

Photodegradation of visible light-excited organic pollutants was used to test the photocatalytic properties of samples prepared for different morphologies. BPA was used as the probe molecule, BOC adsorbed 12% of BPA, and BOI had little adsorption (1%). Although the higher the composition ratio of BOC, the stronger the dark adsorption of BPA, but the difference was not significant (BOC/BOI-1, BOC/BOI-2, BOC/BOI-3 adsorbed 6%, 11% and 12%, respectively), so the adsorption effect of the photocatalyst on BPA was neglected. Photocatalytic BPA removal of 25%, 42%, 100%, 50% and 33% for BOC, BOC/BOI-1, BOC/BOI-2, BOC/BOI-3 and BOI under  $\geq 420\text{nm}$ , which indicates that the photoactivity of the heterojunction is significantly stronger than that of the pure substance. The fitted curves in Figure S11b shows that the degradation of BPA by samples prepared can be further evaluated by the pseudo first order kinetic equation.

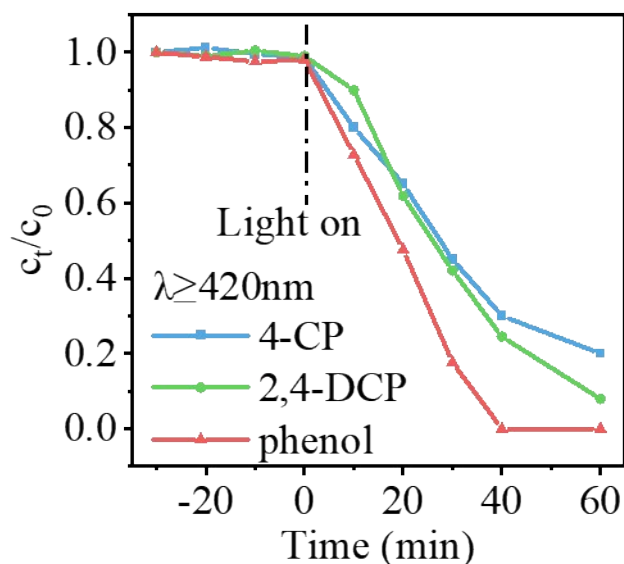


Figure S12. Photocatalytic degradation of 4-CP, 2,4-DCP and phenol (10mg/L) under visible light ( $\lambda \geq 420\text{nm}$ ) irradiation for BOC/BOI-2.

The photodegradation effect of heterojunction on other organic micro-pollutants was studied by selecting BOC/BOI-2 with the best degradation of BPA. Figure S12 shows its photocatalytic universality for 4-CP, 2,4-DCP and phenol. In 60 min, the removal rate of these pollutants by BOC/BOI-2 reach 80%, 93% and 100%, demonstrating the universality of BOC/BOI-2 for photodegradation of organic pollutants.



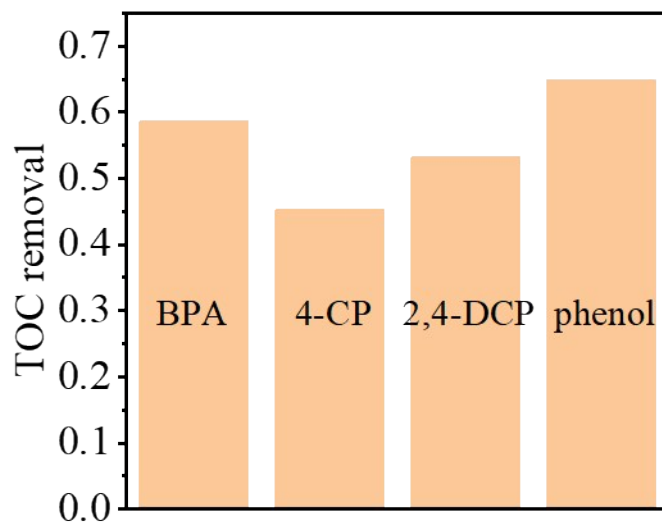


Figure S13. TOC removal rate for BOC/BOI-2

The salinity is an important criterion for measuring the application of photocatalysts in environmental restoration. We selected the prepared photocatalyst BOC/BOI-2 with the best photoactivity to test its salinity for different pollutants under visible light. The TOC removal rates for BPA, 4-CP, 2,4-DCP, and phenol in 60 min were 58%, 45%, 53%, and 65%, respectively.

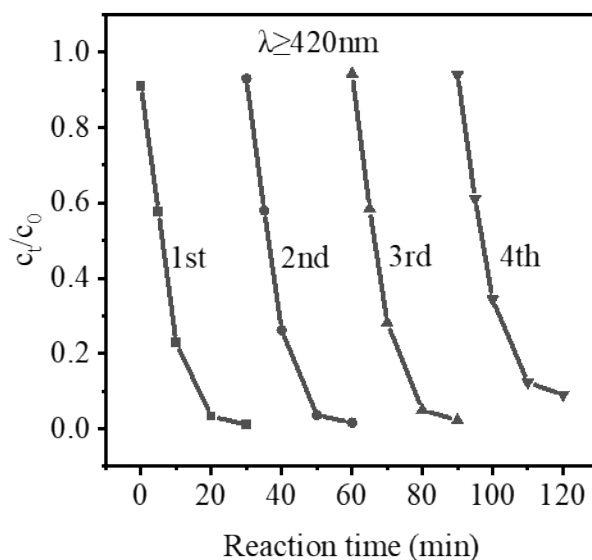


Figure S14. BPA removal in the repeated tests over the BOC/BOI-2

The recoverability and stability of photocatalyst is a nonnegligible indicator to measure the photocatalytic economy. When BOI and BOC form a nano heterojunction with a carbon source ratio of 0.5, the photocatalyst can be reused for 4 times, and the BPA can still be degraded to 9% within 30 minutes under visible light irradiation.

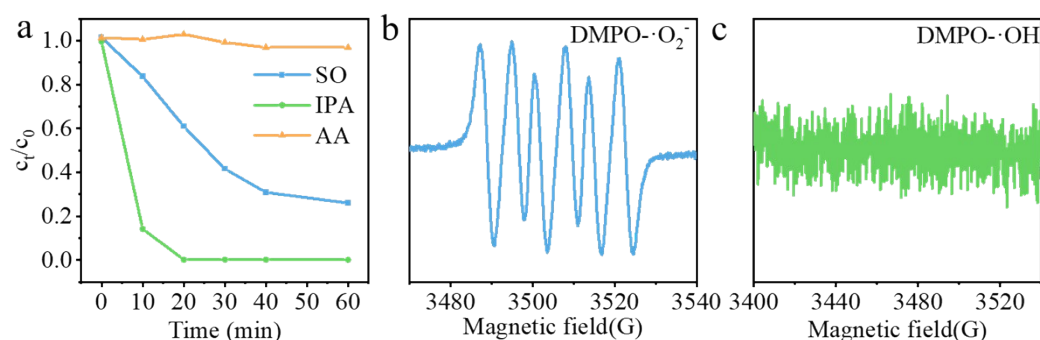


Figure S15. (a) Photocatalytic degradation of BPA over BOC/BOI-2 under visible light irradiation in the presence of different scavengers. (b) The EPR spectra of DMPO-·O<sub>2</sub><sup>-</sup> and (c) DMPO-·OH in the presence of BOC/BOI-2 under visible light irradiation.

In order to evaluate the contribution of oxygen species to the photocatalytic degradation process, typical quenching tests and EPR tests were performed. In the quenching test, we used isopropanol (IPA) as a scavenger for ·OH radicals, ascorbic acid (AA) as a scavenger for ·O<sub>2</sub><sup>-</sup> radicals, and sodium oxalate (SO) as a scavenger for holes. Figure S15a shows that BPA is hardly degraded when 5 mM AA is added to the reaction solution. But when 5 mM SO was added, BPA could still be degraded to 26%. On the other hand, the addition of 5 mM IPA had little effect on the degradation of BPA. The quenching test shows that ·O<sub>2</sub><sup>-</sup> radical is the main active species in the photocatalytic process, and the influence of holes is small. EPR further determines the free radicals generated by the photocatalytic degradation process. As shown in Figure S15b, after visible light irradiation, the six signal peak spectra with almost the same intensity ratio can be clearly observed, which is attributed to the characteristics of DMPO-·O<sub>2</sub><sup>-</sup> adduct, while not obtaining the signal of DMPO-·OH adduct (Figure S15c). The EPR results confirmed that ·O<sub>2</sub><sup>-</sup> radicals were generated during the photodegradation of BOC/BOI-2 heterojunction, and no ·OH radicals were produced, which is

consistent with the results of the quenching test. The above analysis shows that  $\cdot\text{O}_2^-$  is the main active species in the photocatalytic process of BOC/BOI-2, while hole has little effect on it, and  $\cdot\text{OH}$  radical has no effect.

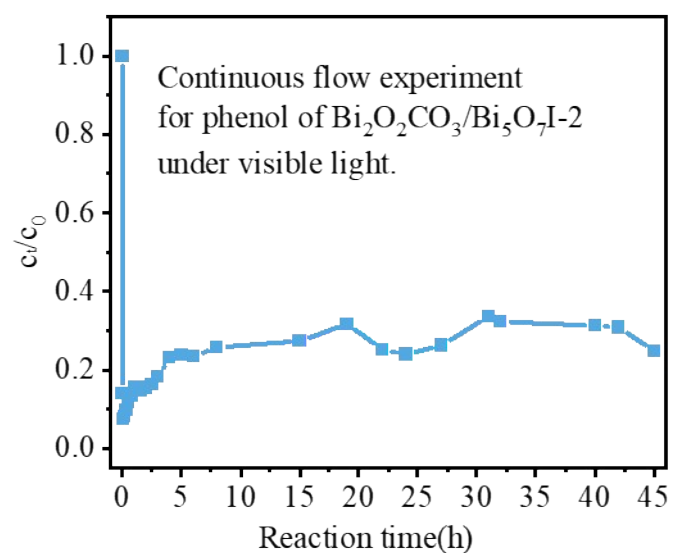
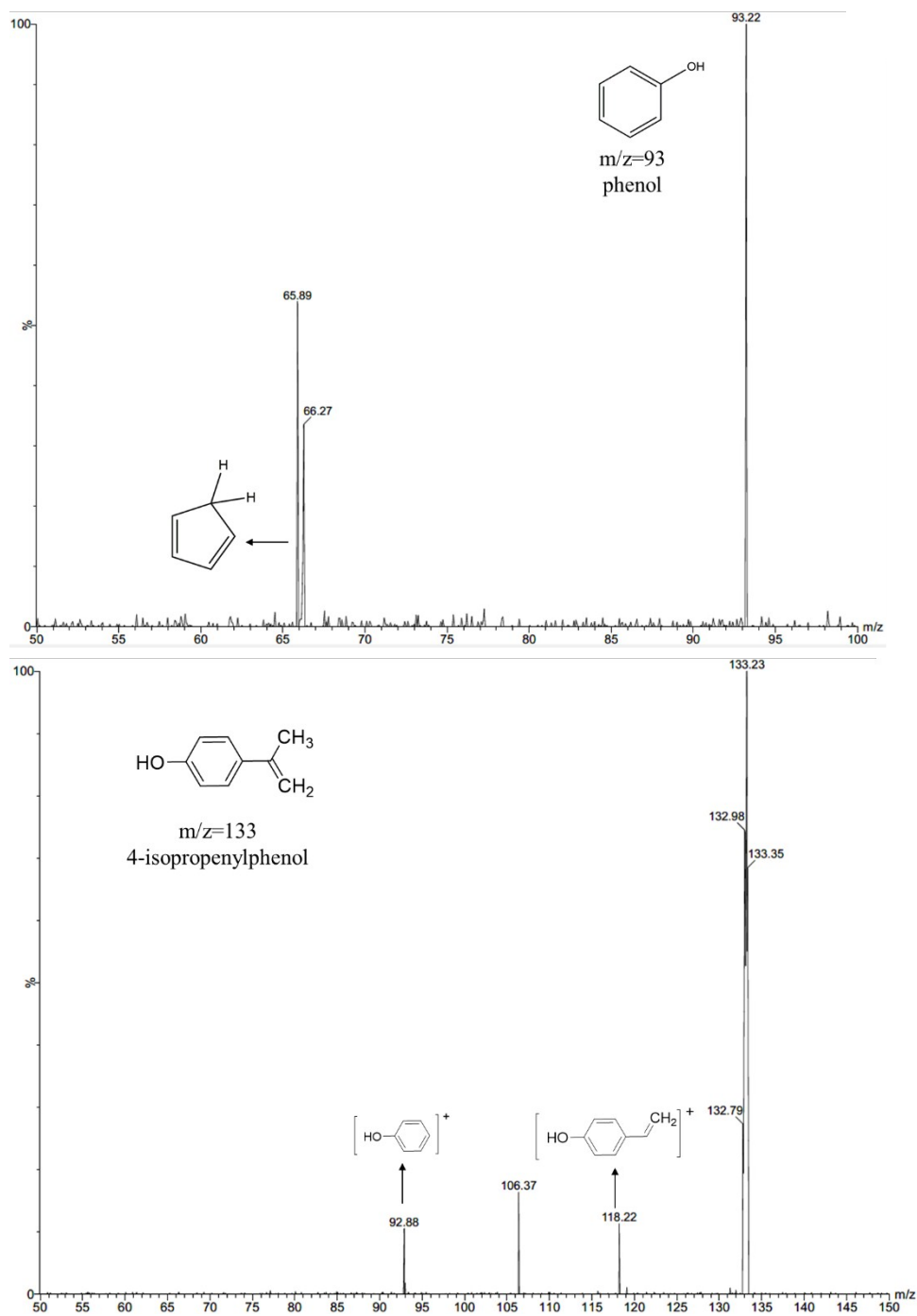
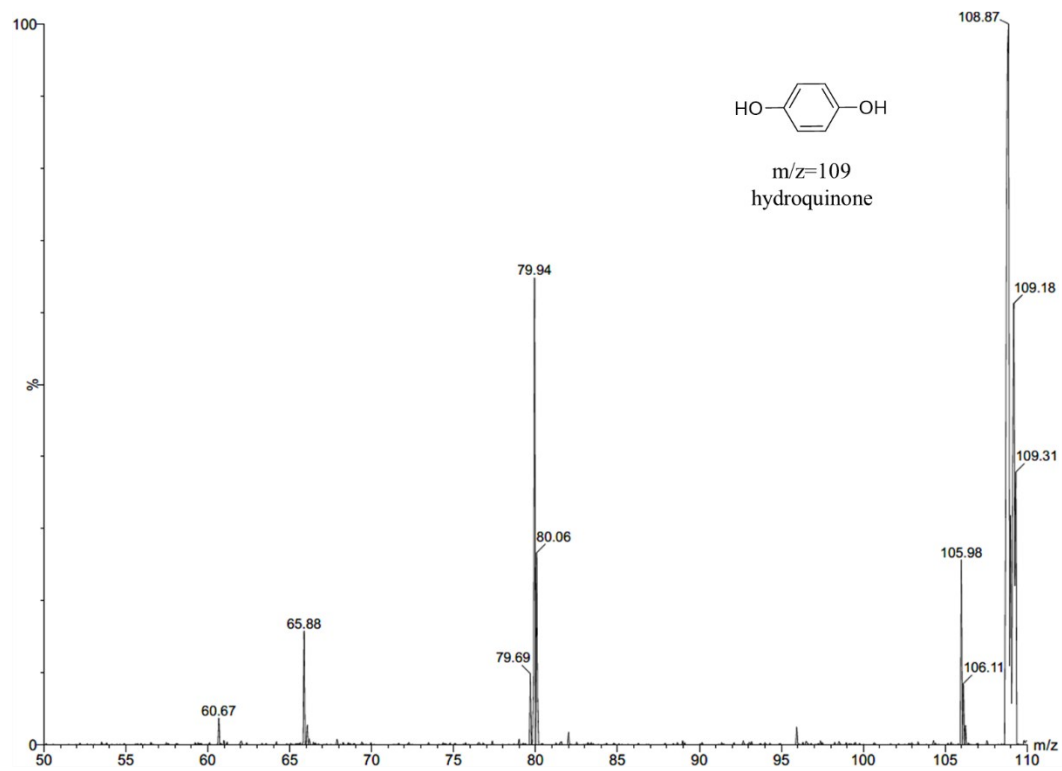
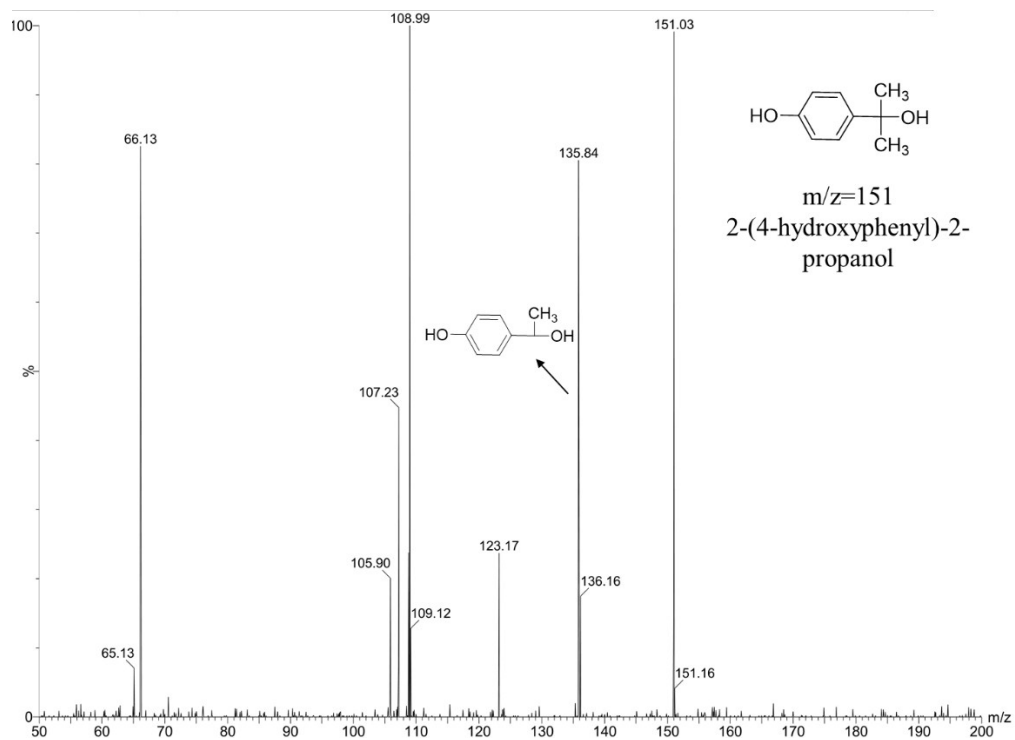


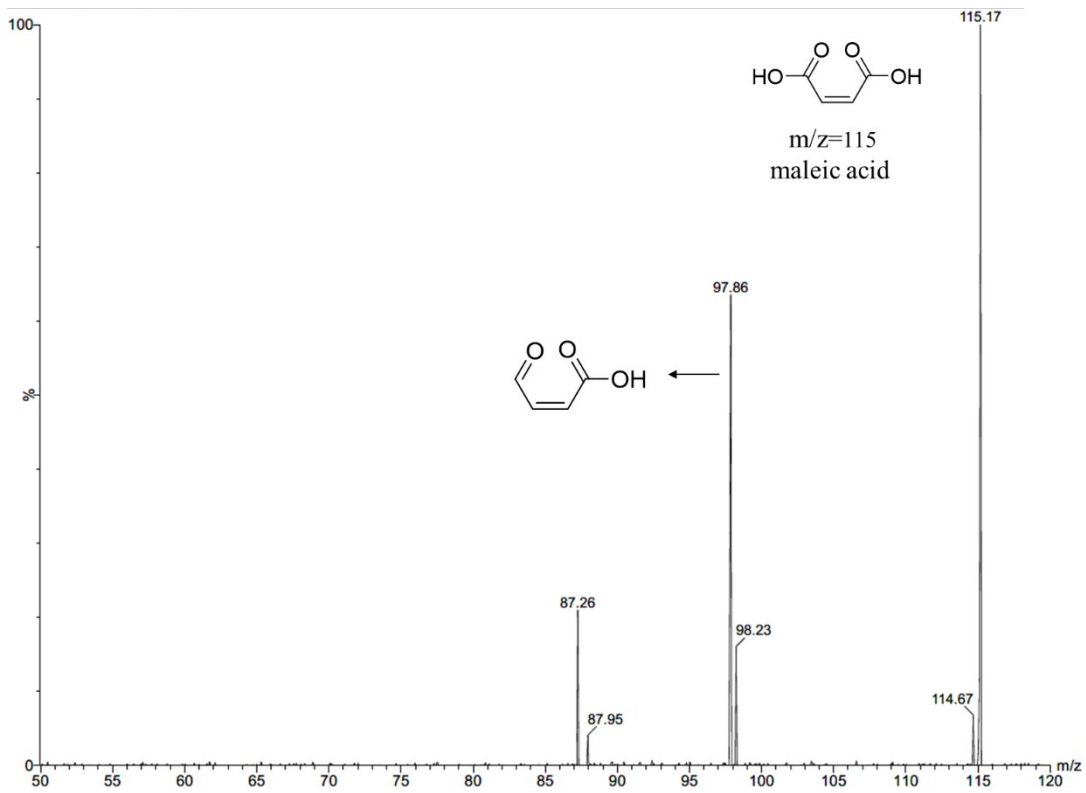
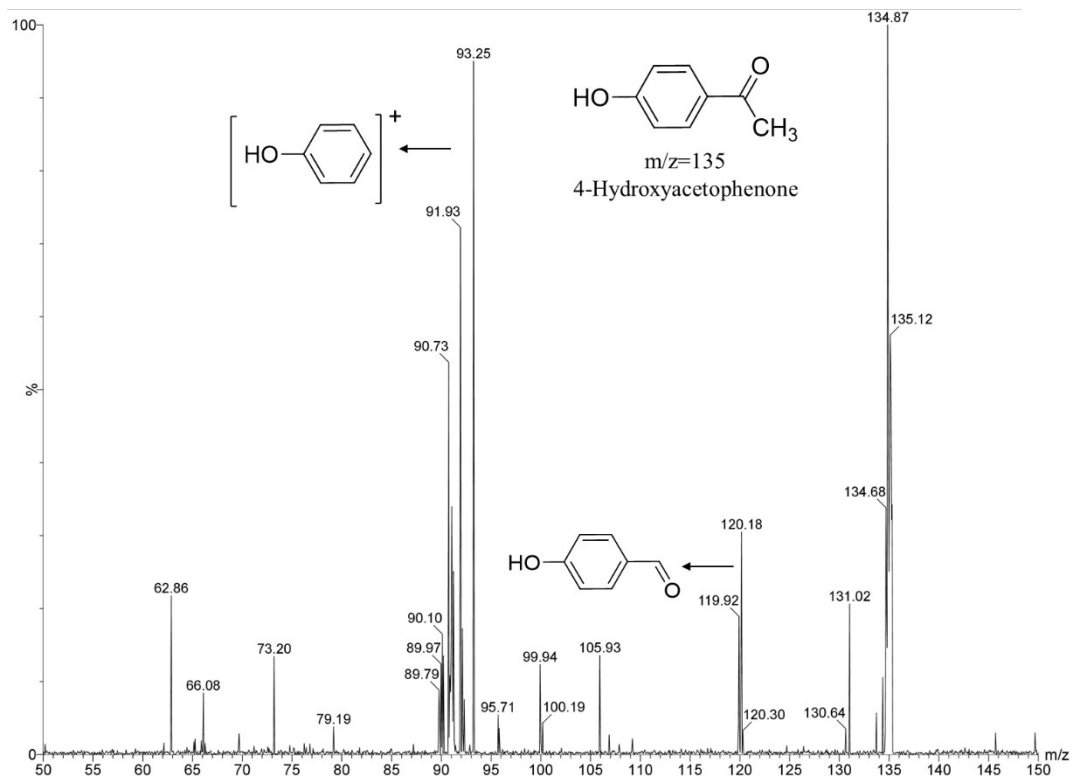
Figure S16. Continuous flow experiments of photocatalytic degradation 10ppm phenol over BOC/BOI-2 under visible light irradiation with 1 mL/min flow rate.

## 1.5 Identification for the intermediates of BPA degradation in $\text{Bi}_2\text{O}_2\text{CO}_3/\text{Bi}_5\text{O}_7\text{I-2}$ system

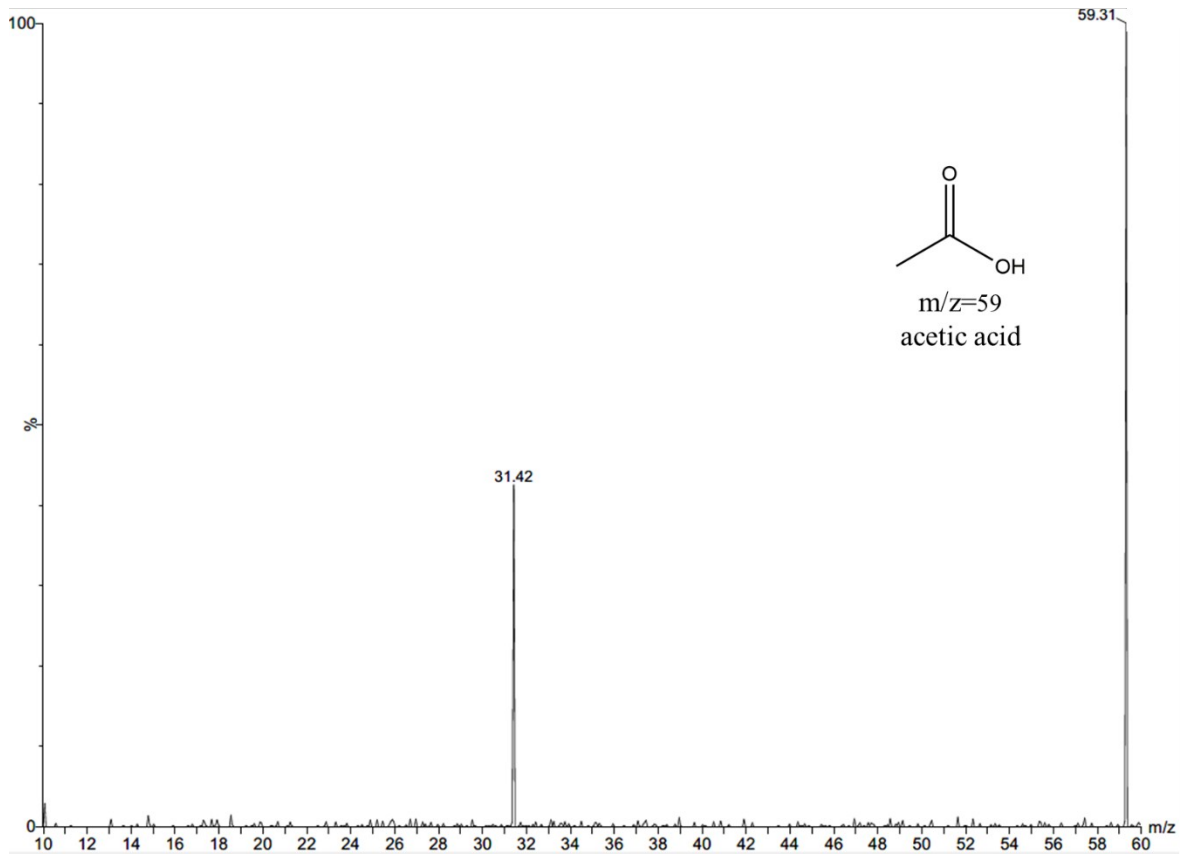
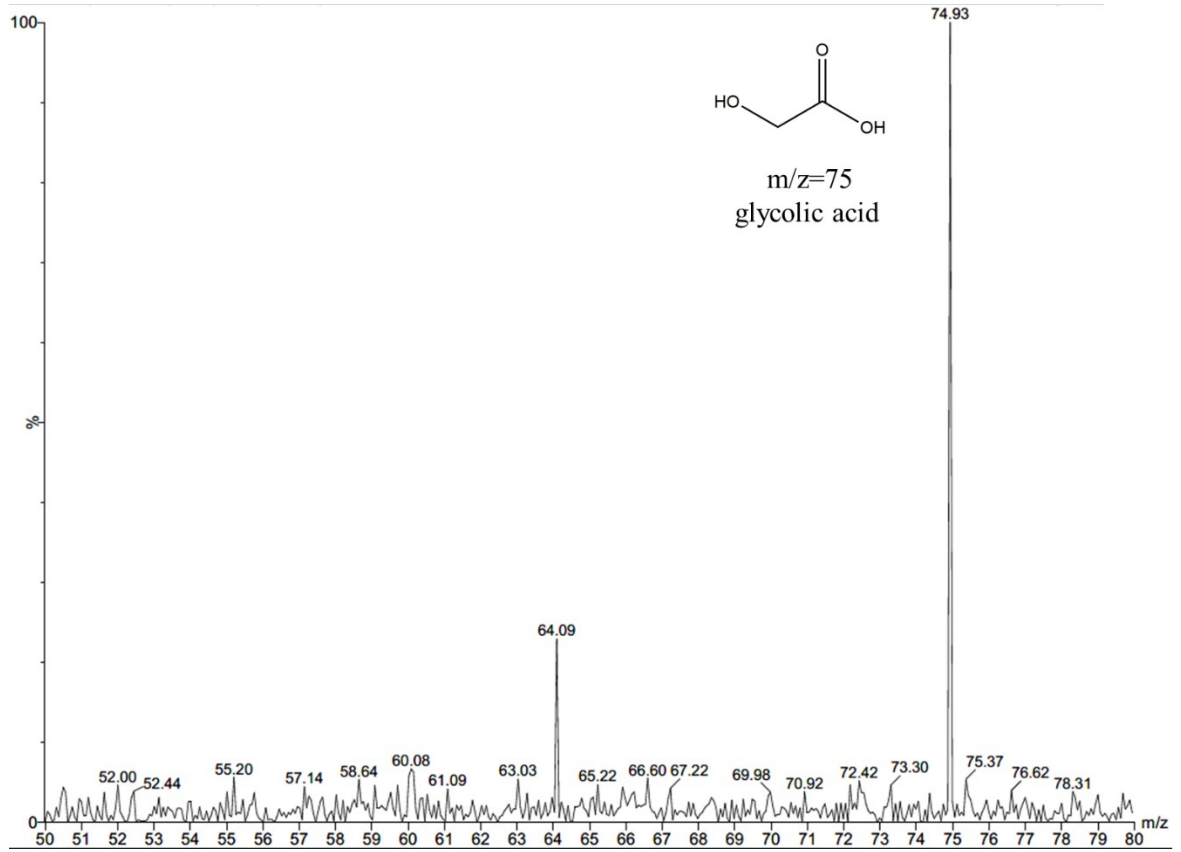
under  $\lambda \geq 420$  nm irradiation (Fig. S17)











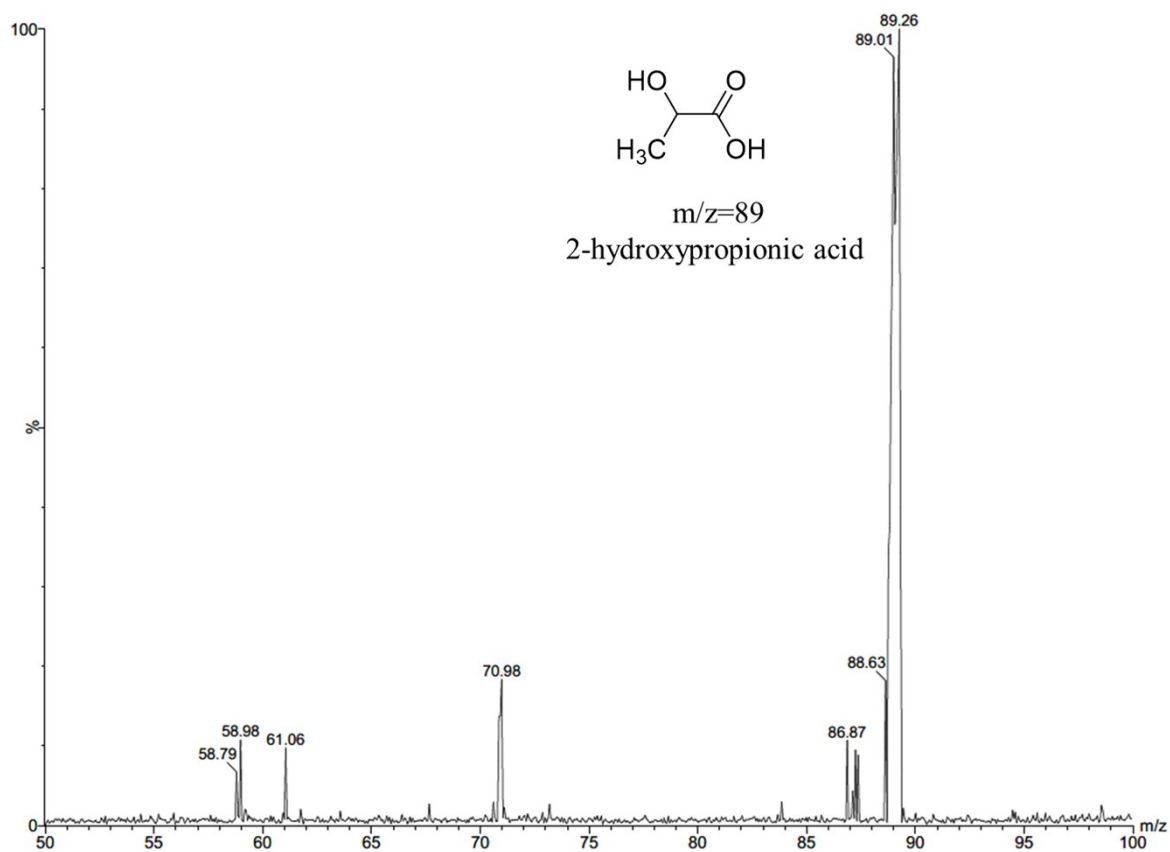


Figure S17. MS/MS chromatograms for the intermediates of BPA degradation in the  $\text{Bi}_2\text{O}_2\text{CO}_3/\text{Bi}_5\text{O}_7\text{I-2}$  system under  $\lambda \geq 420$  nm irradiation.

**1.6 Support for carrier lifetime of  $\text{Bi}_2\text{O}_2\text{CO}_3/\text{Bi}_5\text{O}_7\text{I-2}$  (Figure S18)**

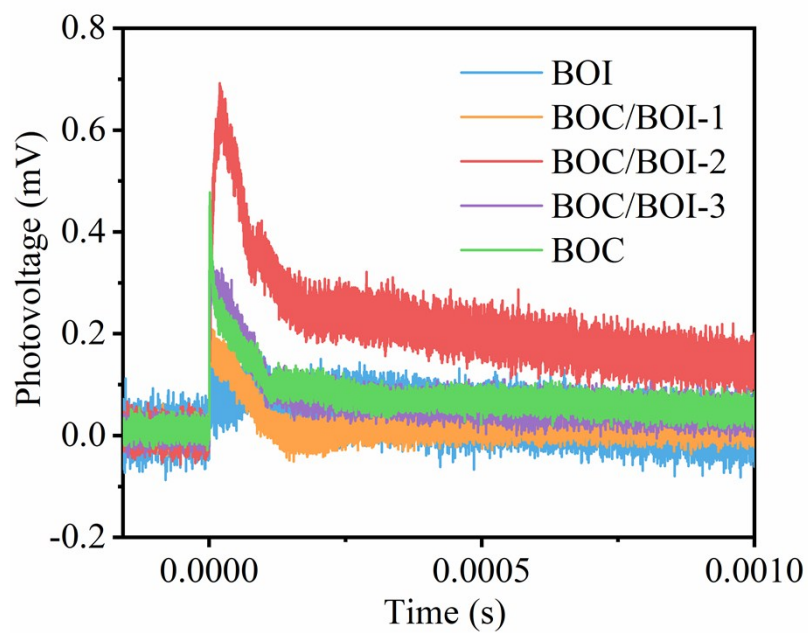


Figure S18. The lifetime of photogenerated holes detected by time-resolved SPV.

## 1.7 Schematic diagram of BOC / BOI heterojunction efficient photocatalysis (Figure S19)

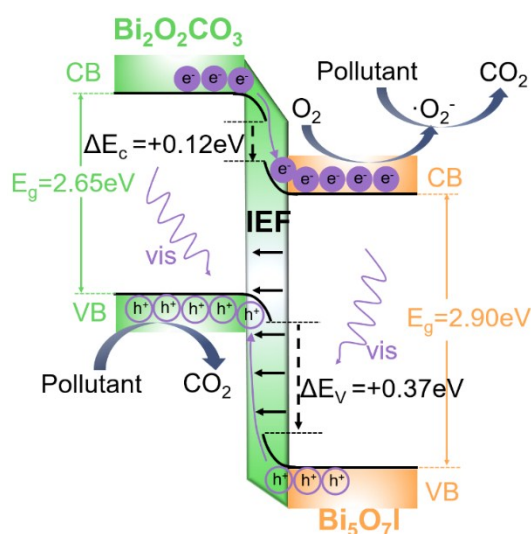


Figure S19. Schematic illustration for the transfer and separation of charge carriers on BOC/BOI heterojunction photocatalyst under visible light irradiation.

Based on the above discussion, photogenerated charges transfer diagram of BOC/BOI-2 with high photocatalytic activity is obtained (Figure S19). Dual drivers by the interfacial energy band offset and the electric field, the charges excited by visible light move along lots of Bi-O chemical bonds bridge, realizing high-flux photogenerated charge drift. Finally,  $\cdot\text{O}_2^-$  radicals and holes are accumulated in the CB of BOI and VB of BOC, respectively, which oxidize pollutants to  $\text{CO}_2$  to complete a highly efficient photocatalysis.

## 2. Supporting tables

Table S1. Mulliken atomic charge of Bi in BOC at the interface of heterojunction

Species	s	p	d	f	Total	Charge(e)
Bi 1	1.87	1.89			3.76	1.24
Bi 2	1.81	1.79			3.60	1.40
Bi 3	1.79	1.77	0.00	0.00	3.56	1.44
Bi 4	1.87	1.79			3.66	1.34
Bi 5	2.05	2.00			4.05	0.95
Bi 6	2.08	2.12			4.20	0.80

As shown by the Mulliken atomic charge of Table S1, the electron amount of Bi 1~4 in this interface is greatly increased compared with Bi 5~6, that is, the static charge is significantly reduced (indicating that the calculated electron amount increases the electron amount  $q$  than the isolated atom, it means that the static charge of the atom in the molecule is  $-q$ ). This is because the distance between Bi 1-4 in BOC and O 1~4 in BOI is short at the interface, and the electronegativity of Bi in BOC is less than O, on which the charge is easily attracted by O, so that the static charge of Bi 1~4 is significantly reduced compared with Bi 5~6.

Table S2. Chemical bond levels at the heterojunction interface

Bond	Population	Length (Å)
Bi 1-O 1	0.16	2.31
Bi 2-O 2	0.14	2.32
Bi 3-O 3	0.08	2.76
Bi 4-O 4	0.1	2.56

The bond level indicates the strength of the bond between two adjacent atoms and Non-zero bond levels indicate that there is a chemical bond between the corresponding atoms. The larger the bond level, the more stable the bond. Bi 1-O 1 and Bi 2-O 2 having large bond level means that the chemical bond is more stable than that of Bi 3-O 3 and Bi 4-O 4.

Table S3. Lifetimes of time-responsive fluorescence spectrum of as-prepared samples under 250 nm irradiation

Sample	$\tau_1$	$\tau_2$	$\tau_3$	$\tau_{av}$ (ns)
BOI	0.13 (14%)	0.14 (52%)	12.2 (34%)	0.58
BOC/BOI-2	0.17 (3%)	5.57 (59%)	58.02 (38%)	2.93
BOC	0.14 (36%)	0.15 (51%)	14.42 (13%)	0.68

a) The average lifetime ( $\tau_{av}$ ) was then determined using the equation:

$$\tau = \frac{\sum_{i=1}^n a_i \tau_i^2}{\sum_{i=1}^n a_i \tau_i}$$

Table S4. Lifetimes of the time-resolved SPV decays of as-prepared samples under 350 nm Irradiation.

Sample	Peak 1		Peak 2		Peak	
	$\tau_1$ (s)	Intensity (mV)	$\tau_2$ (s)	Intensity (mV)	$\tau_3$ (s)	Intensity (mV)
BOI	–	–	–	–	1E-4	0.13
BOC/ BOI-1	8E-7	0.22	2E-4	0.16	–	–
BOC/ BOI-2	9E-7	0.28	1E-2	0.67	–	–
BOC/ BOI-3	7E-7	0.26	1E-4	0.31	–	–
BOC	–	–	–	–	1E-3	0.47

For heterojunction BOC/BOI-1, 2, 3, there are two photogenerated charge migration processes, named peak 1 and peak 2. Peak 1 is attributed to the photogenerated holes generated by BOI reaching its surface, and peak 2 is the photo-generated holes that migrate to BOC through the bridge under the action of the dual drivers at the interface.  $\tau_1$  and  $\tau_2$  are used to denote the decay times of peak 1 and peak 2 respectively. For pure substances BOC and BOI, only one peak of photogenerated holes reaches the surface, and  $\tau_3$  is applied to represent the decay time. In addition, the peak value indicates the intensity of the surface photovoltage. As far as the intensity of surface photovoltage is concerned, BOC / BOI-2 has the strongest signal for peak 1 or peak 2, indicating that the most photo-generated holes reach its surface. As far as the decay time of surface photovoltage is concerned, although the decay time of peak 1 is not much different, BOC / BOI-2 has the absolute advantage of the slow decay time of peak 2.



**Table S5.** Previous research work on photocatalytic degradation of BPA

Photocatalyst	Photocatalyst dosage and BPA concentration	Additional reagents	Photocatalytic degradation effect	Light source	Reference
Bi <sub>2</sub> O <sub>2</sub> CO <sub>3</sub> / Bi <sub>5</sub> O <sub>7</sub> I	50mg 10ppm	-	40min-99.1%	visible light ( $\lambda > 420$ nm)	This work
2D/2D BiOCl-g-C <sub>3</sub> N <sub>4</sub> untrathin heterostructure nanosheets	50mg 10ppm	-	85min-100%	visible light ( $\lambda > 420$ nm)	3
0.3-Bi <sub>2</sub> MoO <sub>6</sub> /MIL-88B	20mg 20ppm	10mM H <sub>2</sub> O <sub>2</sub>	60min-100%	visible light (760nm $>\lambda > 420$ nm)	4
N-K <sub>2</sub> Ti <sub>4</sub> O <sub>9</sub> /ZIF-8	10mg 10ppm	-	90min-100%	visible light ( $\lambda > 420$ nm)	5
CdS QDs modified surface oxygen vacancy defect ZnO <sub>1-x</sub> -TiO <sub>2-x</sub> solid solution sphere	-	-	210min-99%	visible light	6
C <sub>3</sub> N <sub>4</sub> @Zn-BWO	30mg 10ppm	-	120min-93%	visible light ( $\lambda > 420$ nm)	7
Co-doped MIL-53-NH <sub>2</sub>	50mg 10ppm	-	120min-99.9%	visible light ( $\lambda > 400$ nm)	8
nitrogen-doped graphene/TiO <sub>2</sub>	50mg 20ppm	PMS	60min-100%	a 300 W mercury lamp	9
g-C <sub>3</sub> N <sub>4</sub> -PhA (30)	30mg 20ppm	-	80min-100%	visible light ( $\lambda > 420$ nm)	10
$\gamma$ -Fe <sub>2</sub> O <sub>3</sub> - bentonite	100mg 20ppm	-	300min-61%	visible light	11
Bi <sub>2</sub> S <sub>3</sub> -BiVO <sub>4</sub> graphene aerogel	50mg 10ppm	-	120min-100%	visible light ( $\lambda > 420$ nm)	12

### 3. Reference

- 1 Y. Guo, K. Cui, M. Hu and S. Jin, *Chemosphere*, 2017, **181**, 190-196.
- 2 T. Xiong, H. Huang, Y. Sun and F. Dong, *J. Mater. Chem. A*, 2015, **3**, 6118-6127.
- 3 Q. Wang, W. Wang, L. Zhong, D. Liu, X. Cao and F. Cui, *Appl. Catal. B*, 2018, **220**, 290-302.
- 4 K. Zhao, Z. Zhang, Y. Feng, S. Lin, H. Li and X. Gao, *Appl. Catal. B*, 2020, **268**.
- 5 C. Shao, S. Feng, G. Zhu, W. Zheng, J. Sun, X. Huang and Z. Ni, *Mater. Lett.*, 2020, **268**.
- 6 D. Sun, D. Chi, Z. Yang, Z. Xing, P. Chen, Z. Li, K. Pan and W. Zhou, *J. Alloys Compd.*, 2020, **826**.
- 7 X. Ruan and Y. Hu, *Chemosphere*, 2020, **246**, 125782.
- 8 S. W. Lv, J. M. Liu, N. Zhao, C. Y. Li, Z. H. Wang and S. Wang, *J. Hazard. Mater.*, 2020, **387**, 11.
- 9 Y. Zhao, G. Wang, L. Li, X. Dong and X. Zhang, *Chemosphere*, 2020, **244**.
- 10 F. Ge, Y. Xu, Y. Zhou, D. Tian, S. Huang, M. Xie, H. Xu and H. Li, *Appl. Surf. Sci.*, 2020, **507**.
- 11 Y. Y. Cao, G. Z. Zhou, R. S. Zhou, C. Z. Wang, B. R. Chi, Y. Wang, C. Y. Hua, J. Qiu, Y. Q. Jin and S. Wu, *Sci. Total Environ.*, 2020, **708**, 11.
- 12 Q. Liang, S. Ploychompoo, J. Chen, T. Zhou and H. Luo, *Chem. Eng. J.*, 2020, **384**, 123256.